PNAS
www.pnas.org

Supplementary Information for

Metamorphism-facilitated faulting in deforming orthopyroxene: implications for global intermediate-depth seismicity

Feng Shi, Yanbin Wang, Jianguo Wen, Tony Yu, Lupei Zhu, Taizi Huang, and Kelin Wang

Corresponding Author: Yanbin Wang
Email: wang@cars.uchicago.edu

This PDF file includes:

Supplementary text
Figures S1 to S12
Tables S1 to S2
SI References

Supplementary Information Text

Supplemental Experimental Observations

Typical event location and recorded AE waveforms are shown in Fig. S6. Figure S7 summarizes the mechanical responses of the other four samples that behaved in brittle fashion during the deformation experiments.

Figure S8 summarizes overall sample state after retrieval to ambient conditions. The sample (D2070) which was deformed within the stability field of Opx contained not faults (Fig. S8a). The sample (D2077) that underwent well-developed metamorphic reaction is also fault free (Fig. S8d). The other two samples, D2081 (Fig. S8b) and D2069 (Fig. S8c), were deformed in brittle and semi-brittle fashion, respectively.

In Sample D2071 (brittle with well-developed faults), very fine Grt grains (grainsize < 1 μm) form thin layers along boundaries and thin Grt lamellae are exsolved within Opx grains (Figs. S9a, b). Grain orientation spread (GOS) maps show that there is virtually no sub-grain development in large Opx grains, except the breakup of Opx crystals due to Grt and Cpx lamellae, causing mis-orientation up to ~8° (Figs. S9c, e). Vast majority of the grains are within 2°. These observations suggest that the dominant deformation mechanism in Opx is grain boundary sliding. This is not surprising given that virtually all the Opx grain boundaries are "lubricated" by fine-grained Grt. GOS of Grt is difficult to quantify, due to the small grain size. Figs. S9d and f show that relatively larger (> 1 μm) Grt grains also have a narrow GOS. However, given very limited sampling of Grt grains, the GOS measured in Grt may not represent true orientation spread. Fig. S10 is a higher resolution EBSD image, showing spatial distribution of the Grt and Cpx lamellae in deformed Opx.

Grt grains are clearly identified by SAED in the TEM (Fig. S11a). Fault zones typically consist of ultrafine Grt and Al-poor Opx (Figs. S11a, b). High-resolution TEM (HRTEM) reveals extremely thin Cpx domains (~10 nm) around the boundaries of Opx grains immediately adjacent to a micro-fault (Fig. S11c). The (100) planes of Cpx, with a characteristic 9 Å repeat, form an epitaxial relation with $(100)_{\mathrm{Opx}}$ with an 18 Å repeat (inset of Fig. S11c). Such ultra-thin layers of epitaxial Cpx are likely formed from Opx by direct high-stress deformation during faulting. A nanocrack has developed in the grain next to an amorphous layer, suggesting high stress heterogeneities across grains along the fault zone.

In the sample (D2069) that was deformed in semi-brittle fashion, Grt-exsolution reaction has essentially engulfed all the Opx grain boundaries (Fig. S12a). Numerous microcracks are present within the Opx grains (Fig. S12b), causing the large number of small AEs.

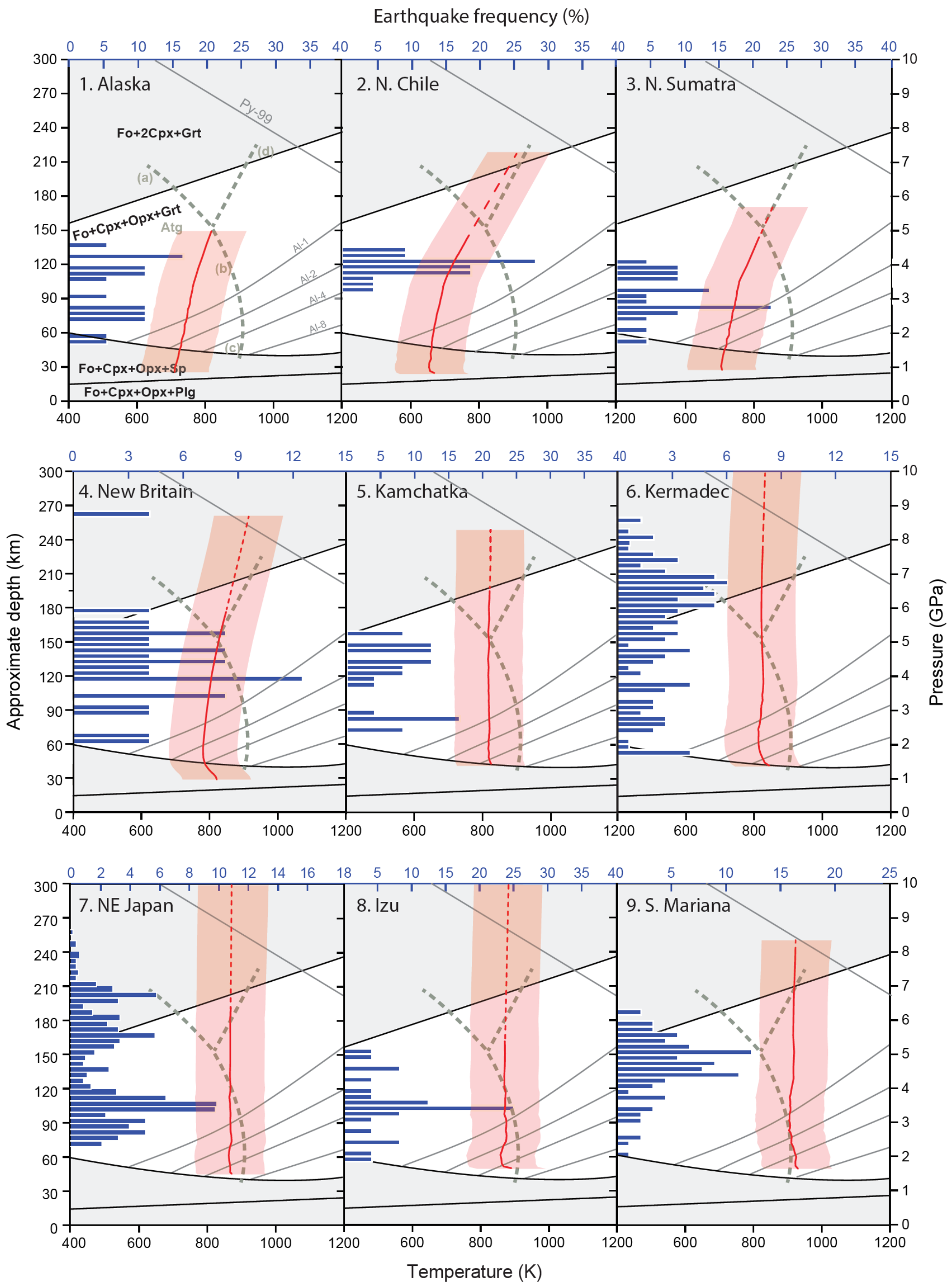

Fig. S1. **Depth distribution of seismic activity and temperature trajectories of the 9 LBSs.** Slabs are plotted in order of increasing age. Most seismic data are from (*1*), except for NE Japan, which is from Ref (*2*). Horizontal blue bars are percentage of seismicity per 5 km depth interval. Most of the seismicity distribution is from (*1*), where numbers of earthquakes selected were limited for reasons state in Supplementary note 1, except for NE Japan (*2*). Red lines are the temperatures of the LBSs from the thermal models, same as those shown in Fig. 1, with the solid part within the DSZ extent, and dashed part beyond the DSZ. Shaded band represents range of deviation from the average due both to temperature uncertainties and to the finite-width of the LBSs. Superimposed are the phase relations shown in Fig. 1.

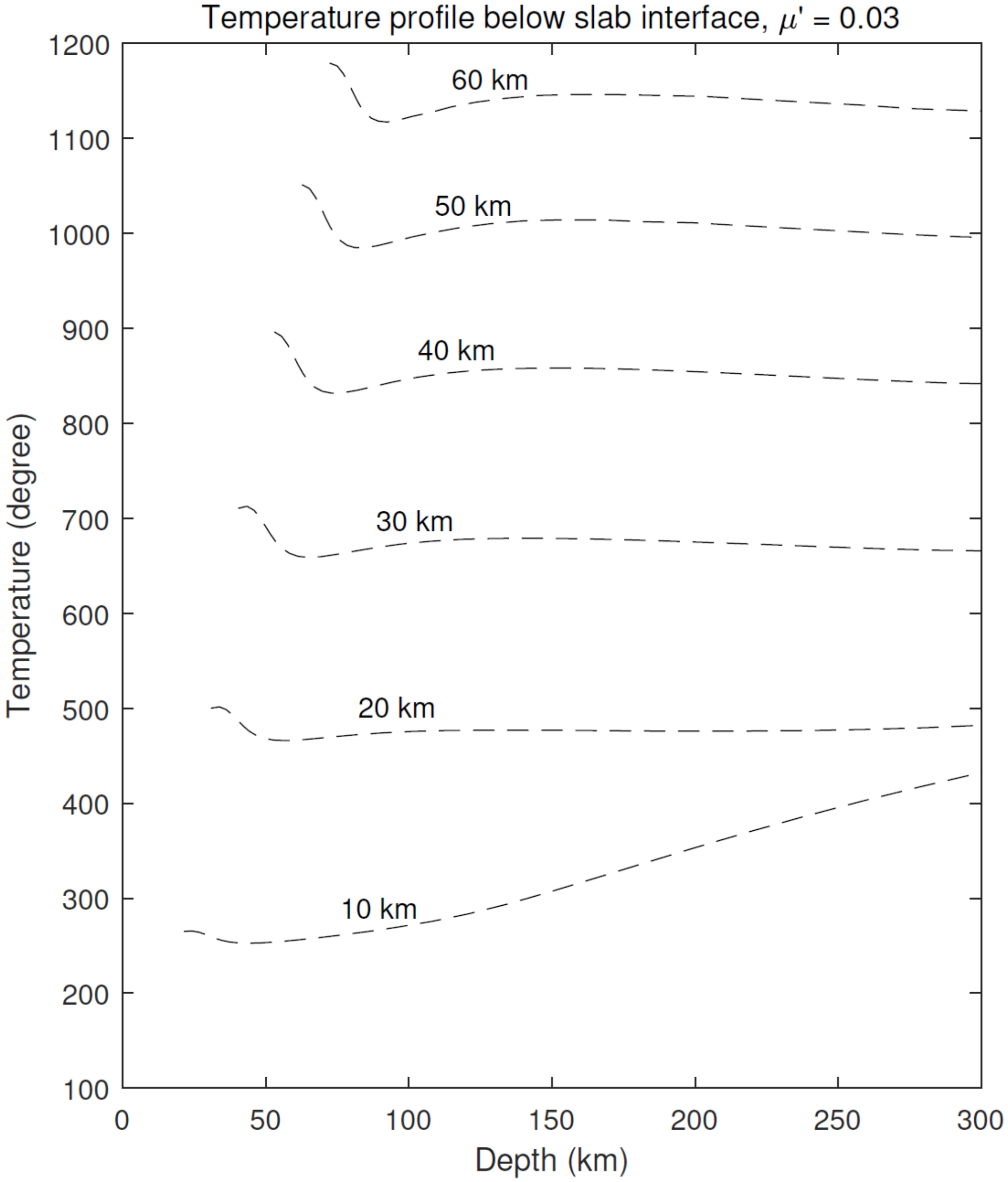

Fig. S2. Temperature profiles under the slab surface for New Britain. Plotted here are depth profiles of temperature at 10 km intervals from 10 to 60 km below the slab surface. According to Table S1, the separation between UBS and LBS is 12 km. The LBS temperature is therefore interpolated from data shown here at 15.5 km depth below the slab surface, (i.e., by taking the UBS-LBS separation to be from 3.5 to 15.5 km below the slab surface).

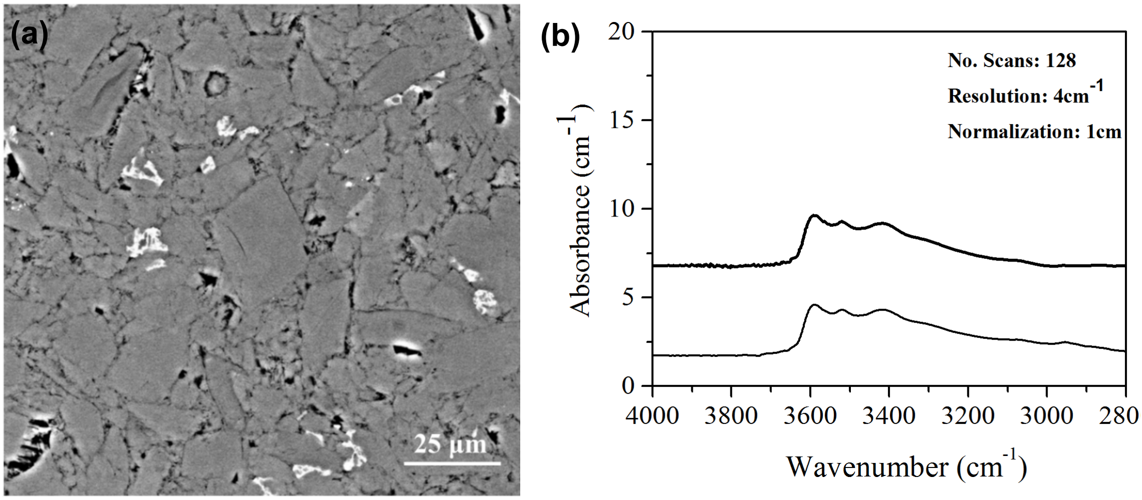

Fig. S3. **Microstructure of the starting material and water content**. **(a)** Microstructure of the starting material, showing mostly straight grain boundaries. Some ilmenite ($FeTiO_3$) needles are also present (bright contrast). The average grain size is 23-38 µm. **(b)** Representative FT-IR spectra taken from the starting material, showing an average water content of about 63 ppm.

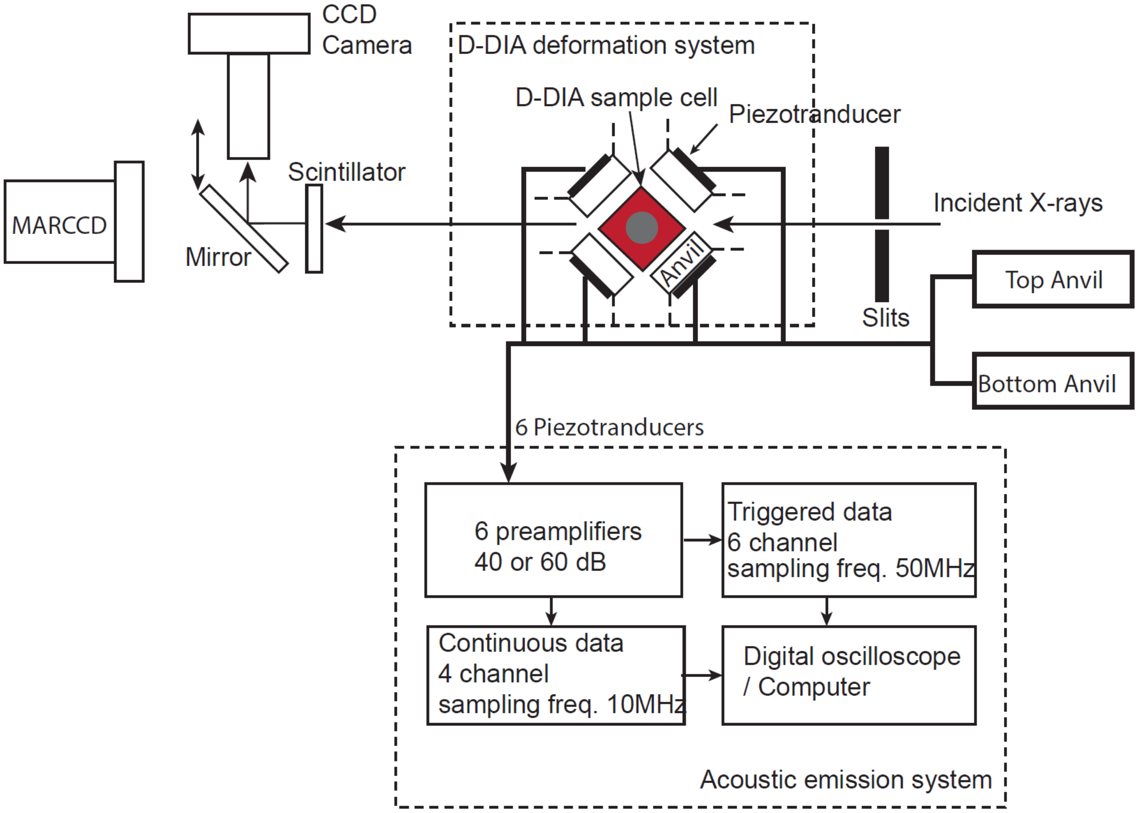

Fig. S4. **Experimental setup.** The D-DIA apparatus is viewed from the top down, with four horizontal anvils. Top and bottom anvils are not shown. The two anvils in dark grey are sinter-diamond (SD) and the other 4 are tungsten carbide (WC). AE transducers (PZT) were attached to the back end of each anvil for AE monitoring. AE signals were amplified by preamps by 60 dB and recorded by 6 digital oscilloscopes. The imaging optics and diffraction optics were automatically switched during the experiment.

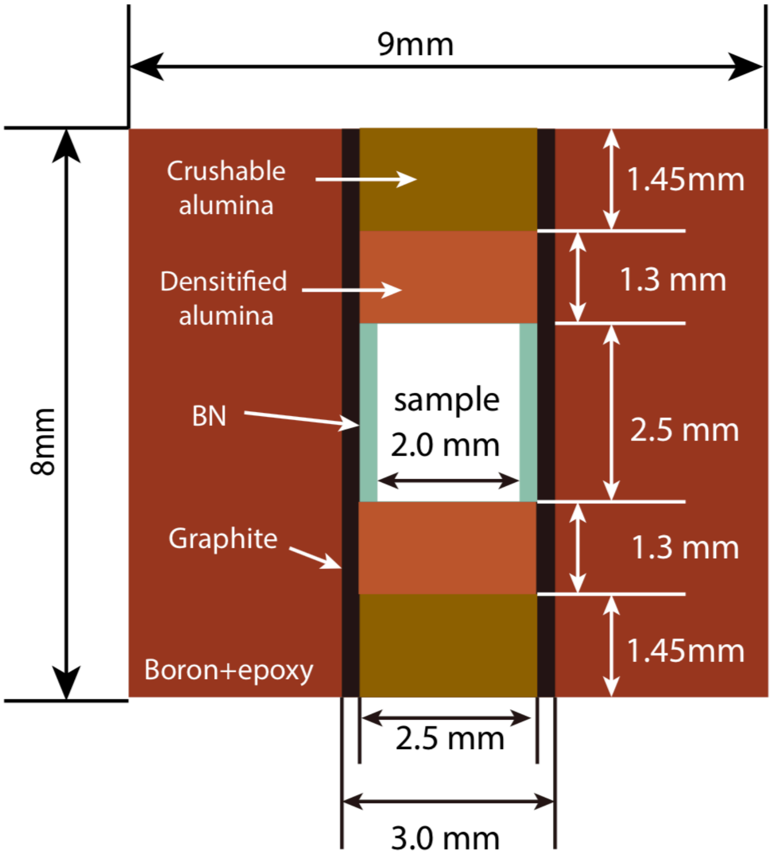

Fig. S5. Cell assembly design for the deformation experiments in the D-DIA. The cubic pressure medium (9x9x8 mm) was made of boron epoxy, and a graphite heater was used to generate high temperatures. Sample was surrounded by a boron nitride (BN) sleeve. Markers (Au foil) were placed at the two ends of the sample for strain measurements using radiography.

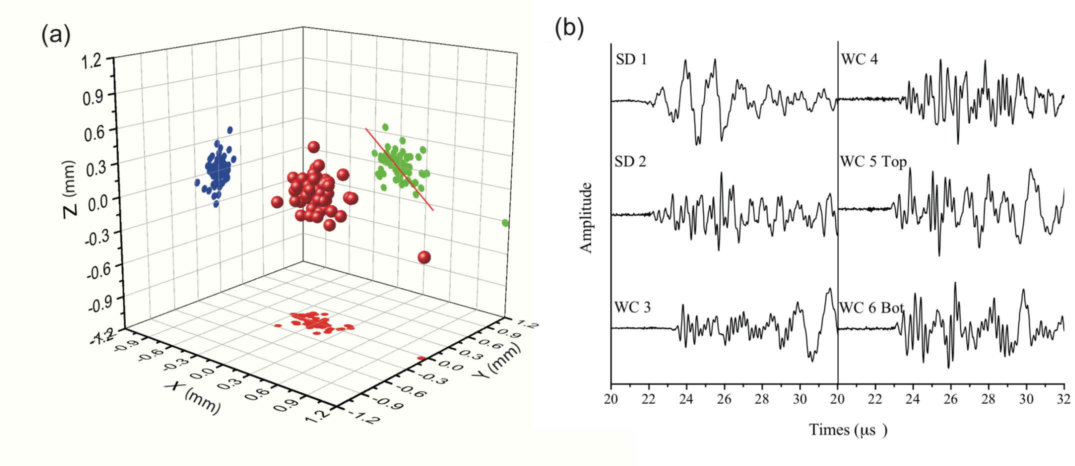

Fig. S6. **Projections of AE locations in D2071 showing distribution of the events. All events are located within the sample**. **(a)** AE events (red solid spheres) form elongated distributions when projected to two of the three perpendicular planes (red dots in the horizontal plane and blue and green dots in the vertical planes). The sample volume after the experiment is approximately outlined as the black dashed cylinder. All AE events are well within the sample boundaries. **(b)** An example of a triggered event in run D2071 (AE record #180), recorded by all six transducers behind six anvils, forming a set of AE waveforms which were used for event relocation analysis.

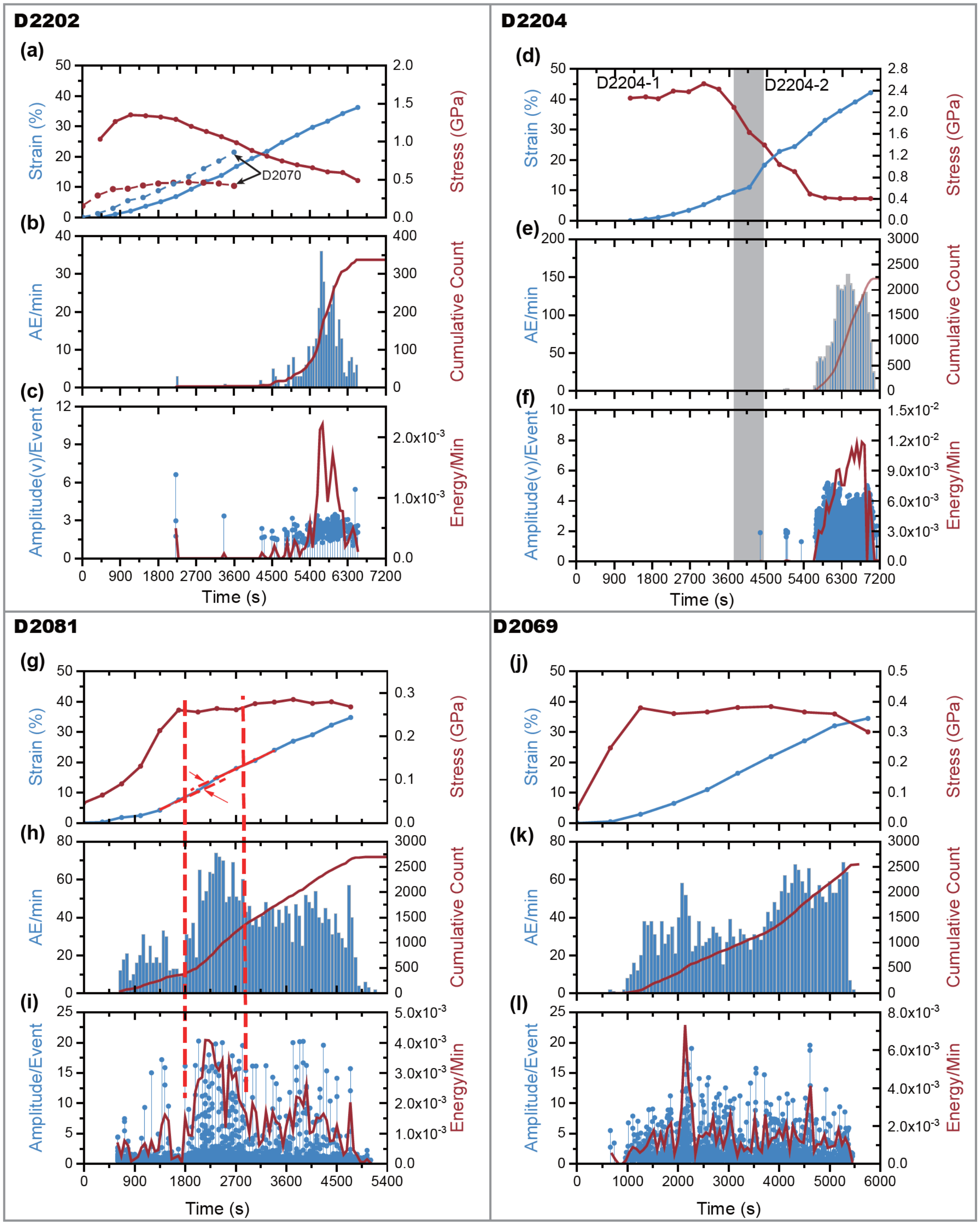

Fig. S7. **Mechanical behavior and AE activity of metastable Opx during deformation.** **(a) – (c)**: D2202 (1173 K). Note continuous decrease in stress in **(a)** after the first AE event at 2250 s **(b, c)**, signifying the onset of Grt precipitation. **(d) – (f)**: D2204-1 (673 K) and D2204-2 (1273 K). No AEs were detected at 673 K, despite the very high differential stress up to 2.6 GPa **(d)**. The grey zone corresponds to temperature ramping from 673 to 1273 K. Stress decreases to ~1 GPa shortly after heating to 1273 K and then drops suddenly to ~0.4 GPa around 5600 s. This stress drop is associated with a strain jump and change in slope around 5600 s. Intense AE bursts occur immediately after 5600 s **(e, f)**. **(g)** – **(i)**: D2081 (1373 K). **(g)** A strain jump around 2200 s is observed (red arrows). **(h)** Peak AE activity is centered around 2200 s, corresponding to the strain jump in **(h)**. **(i)** Energy release rate also peaks around 2200 s, correlating well to the strain jump in **(g)**. **(j) – (l):** D2069 (1473 K). **(j)** The decrease in differential stress near the end is due to termination of deformation, not to macroscopic failure. Red vertical arrow indicates the time when deformation was intentionally stopped. **(k)** AE rate drops off sharply immediately after the termination of deformation. **(l)** Event energies are of similar magnitudes to those in **(i)**; however, this sample has no macroscopic faults when examined in the SEM. The dashed curves in (a) are the stress and strain data from D2070, under conditions where Opx was stable (Table 1). No AE was detected in this experiment.

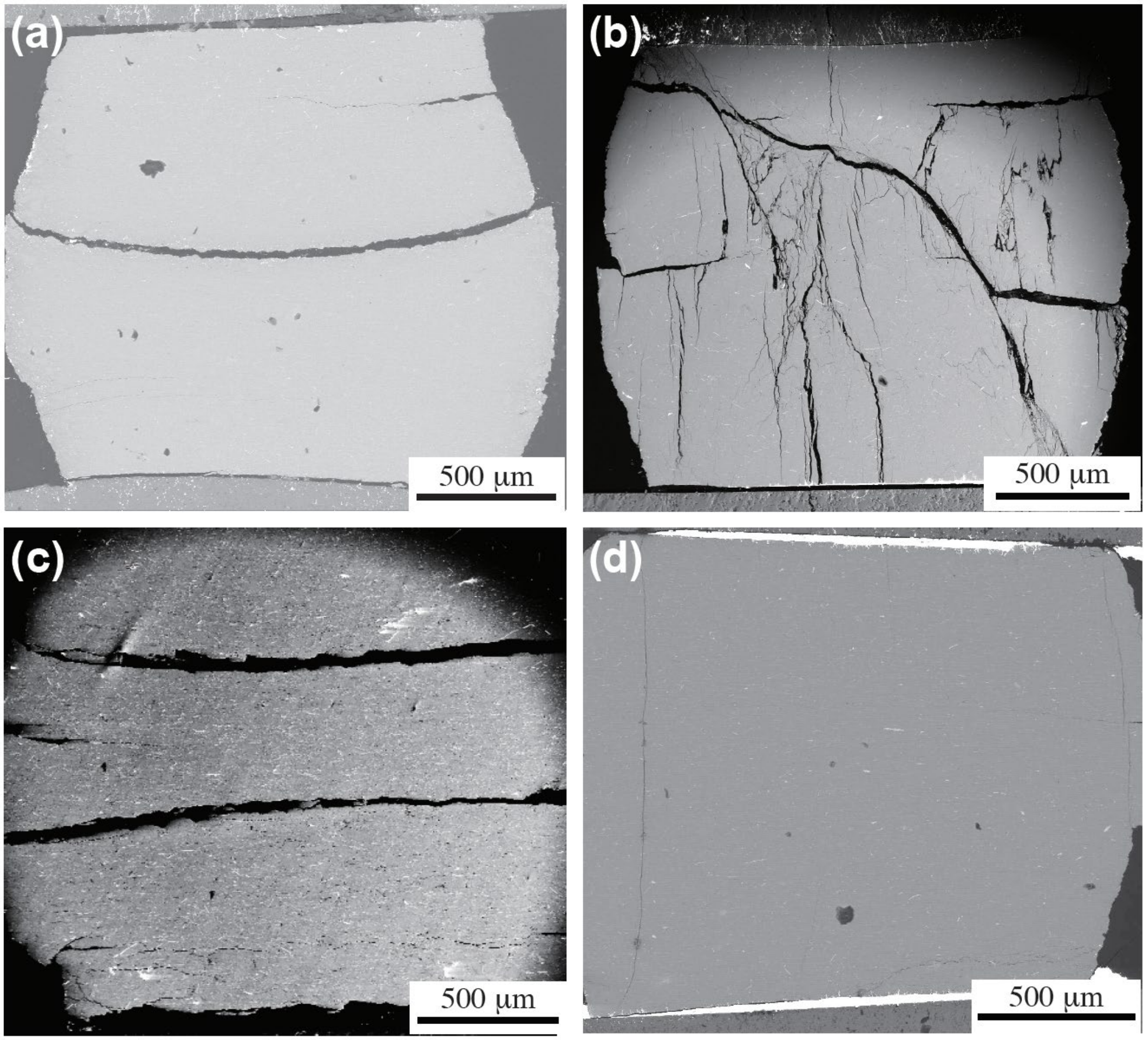

Fig. S8. **Low magnification SEM images of selected recovered samples. (a)** D2070 (1.8 GPa, 1273K). No AEs were detected in this sample, which contains no conjugated faults. The horizontal crack was due to decompression**. (b)** D2081 (4.8 GPa, 1373 K). Numerous AEs were detected. Many faults are present. **(c)** D2069 (5.1 GPa, 1473 K). Numerous AEs were detected but no conjugated faults are present. Horizontal cracks due to decompression. **(d)** D2077 (5.2 GPa, 1523 K). No AEs were detected and no major faults. Thin vertical crack and the small horizontal crack near the bottom are due to decompression.

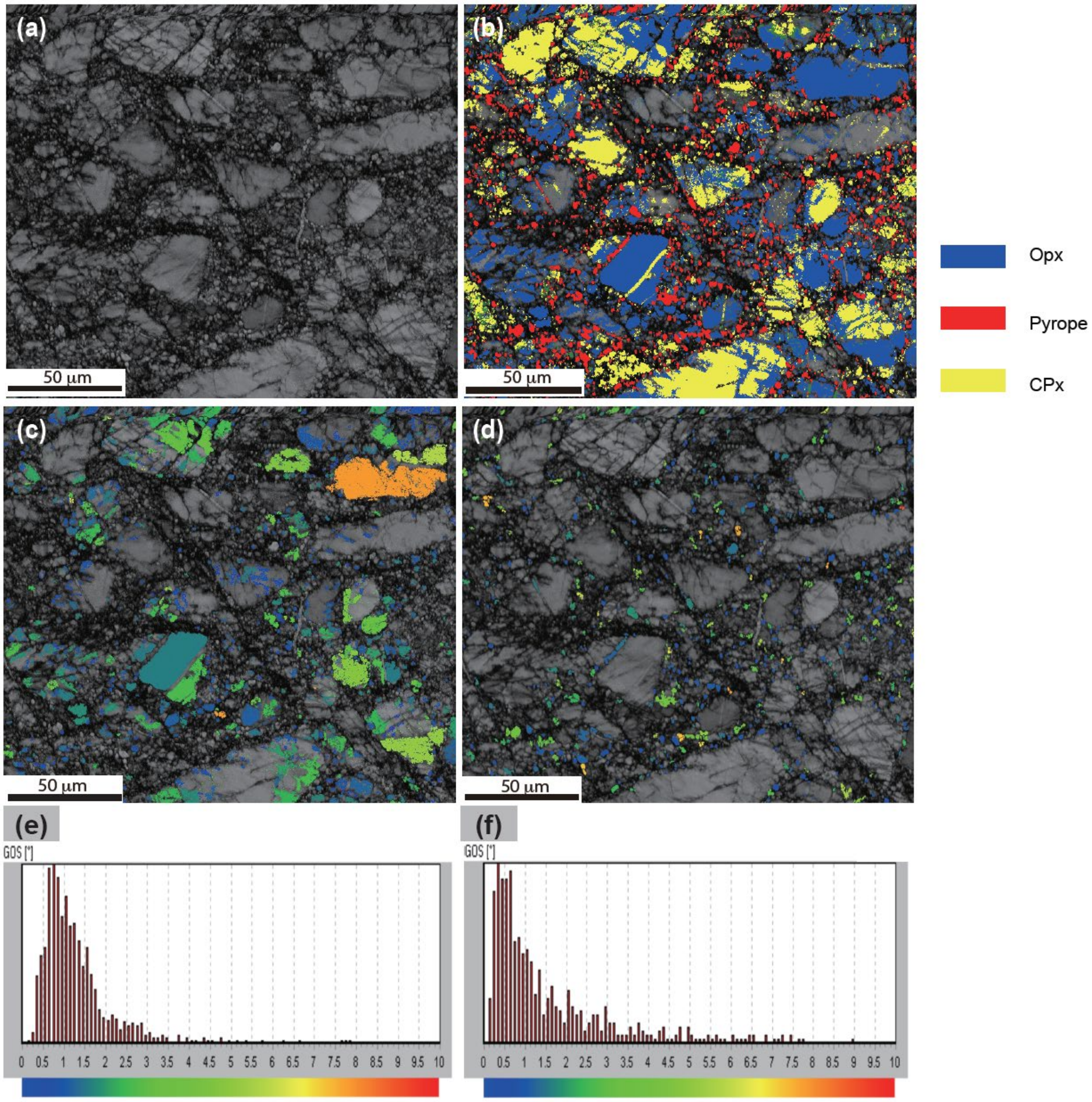

Fig. S9. **EBSD analysis of an area in faulted sample D2071**. **(a)** Band contrast image of the measure region. **(b)** Phase identification. EBSD determined phases are color-coded: Garnet (pyrope) is red, Opx blue, and Cpx yellow. Note Grt grains along all boundaries of Opx grains. Also note garnet lamellae in Opx grains. **(c)** Grain orientation spread (GOS) of the Opx grains. **(d)** GOS of the Grt grains. Colors in (c) and (d) correspond to grain orientation with color scales given under **(e)** and **(f)**, respectively, for Opx and Grt. Both Opx and Grt show very narrow GOS. For Grt, only a small portion of the grains could be measured because most grains are under 1 µm in size, which is beyond EBSD detection limit.

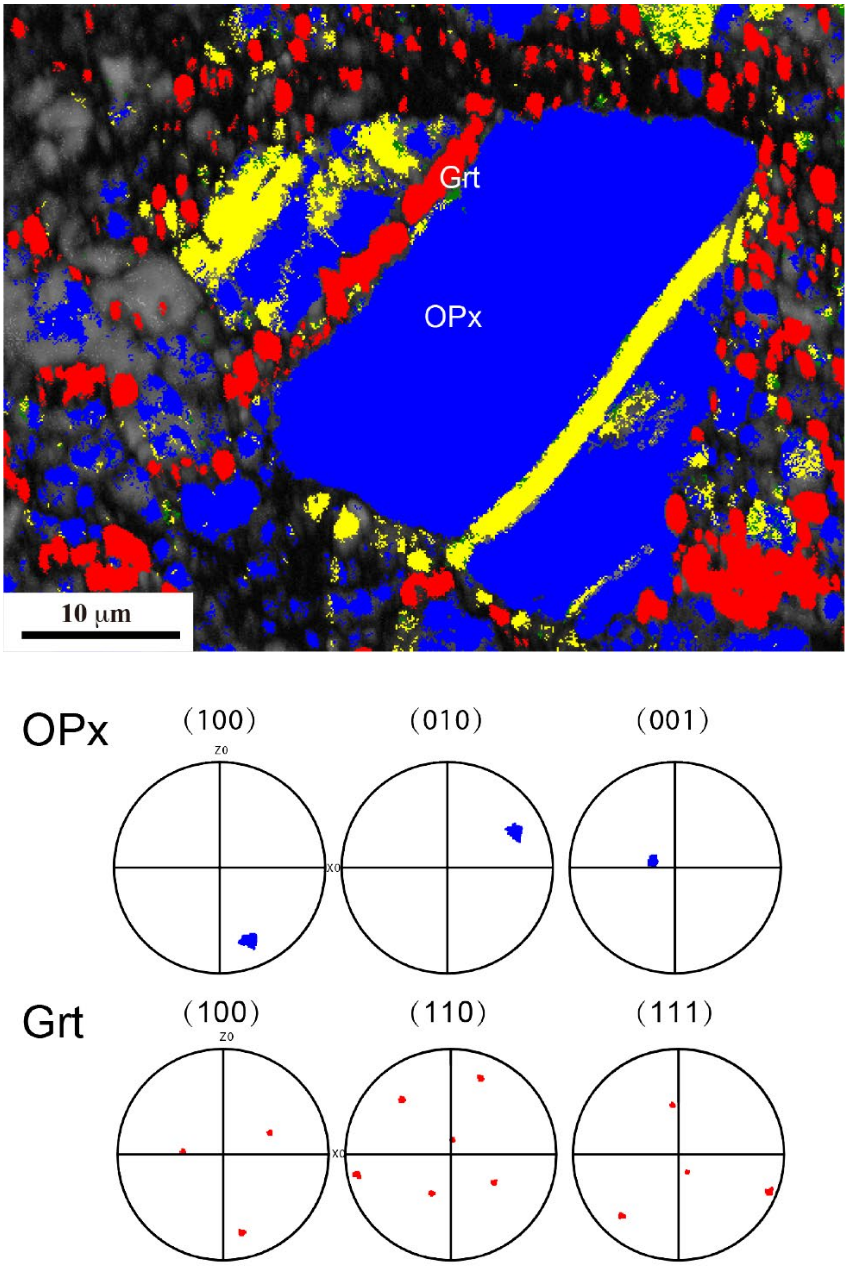

Fig. S10. EBSD analysis of intragranular lamellae and fine-grained reaction products along grain boundaries (D2071). The upper SEM image shows a large Opx grain surrounded by fine-grained material. Three phases are identified by EBSD: Opx (blue), Gart (red), and Cpx (yellow). Note fine-grained Grt (and some Cpx) surrounding the large Opx grain. Within the Opx grain, lamellae of Grt and Cpx are present. While the Cpx lamellae are single-crystal domains within the Opx grain, the Grt lamella is broken into smaller grains. The orientations of the Opx and Grt crystals are given in the lower stereographic projections (upper hemisphere). 4425 Opx measurements show that orientations deviate ever so slightly from a single crystal, whereas 1247 Grt points indicate potential orientational control of the parent Opx phase over orientations of the exsolved Grt. The indices for the large Opx grain show that both Grt and Cpx lamellar are oriented more or less parallel to the $(001)_{\mathrm{Opx}}$.

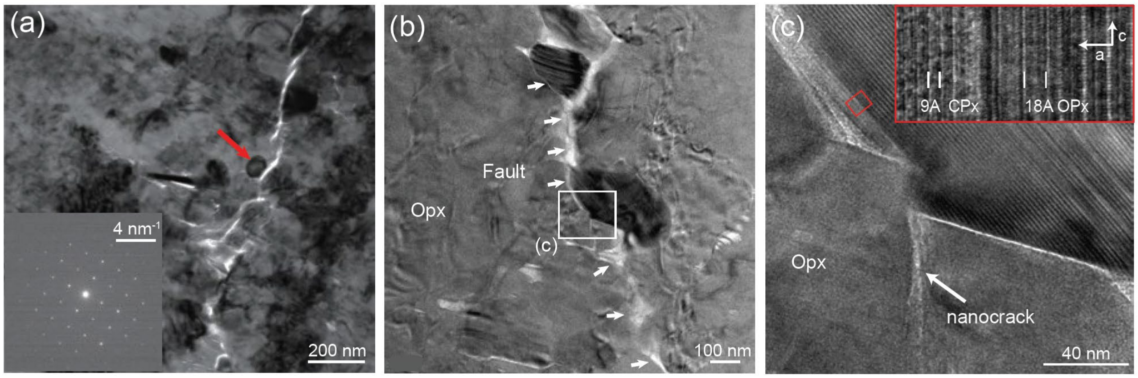

Fig. S11. Typical structure of micro-faults. Bright-field (BF) TEM images. (a) A micro shear zone containing reaction products with grain size on the order of 100 nm. Inset is a SAED pattern, identifying one dark grain (red arrow) as Grt. (b) A micro-fault (white arrows) lined with reaction products with grain size on the order of 100-200 nm. Two small grains are titled with their zone axes nearly parallel to the incident electron beam and appear dark. (c) An enlarged image of the white box in (b), showing a nano-crack in the Opx host grain immediately adjacent to the micro-fault. Inset is a high-resolution TEM (HRTEM) image of (100) lattice fringes in the area indicated by the red box. The 18 Å repeat is characteristic of Opx unit cell. A very thin layer (~15 nm) of 9 Å lattice repeat immediately adjacent to the micro-fault is characteristic of HCpx.

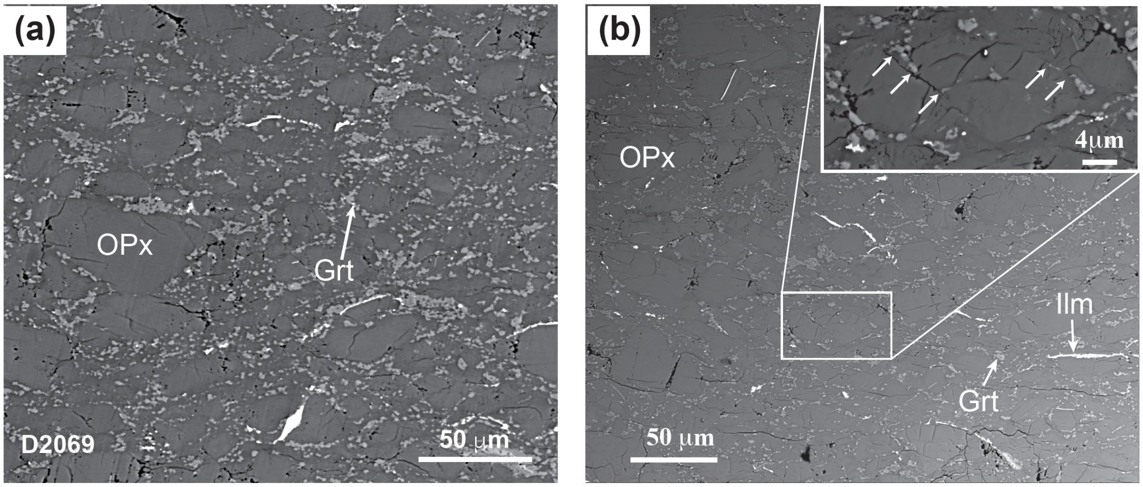

Fig. S12. **Well-developed Grt formation around Opx grains and intragranular cracks in semi brittle sample D2069 (1473 K). (a)** Grt exsolution is well developed, with fine Grt grains outlining all boundaries of Opx grains. Also note numerous intragranular cracks in large Opx grains. **(b)** Fine intragranular cracks are pervasive in large Opx grains. Some localized intergranular shear can also be seen, as indicated by the shear of an ilmenite needle (red arrow). Inset is enlarged image of the boxed area, showing Grt lamellae and associated fractures (white arrows). This sample contains no macroscopic faults. AE amplitudes are controlled by the grain size in this case.

Table S1. Temperatures along the LBS in various subduction zones.

Subduction zone(a)	Lat. °	Long. °	Trench age(b) Ma	Subduct rate(c) km/Ma	DSZ width(d) km	DSZ depth(e) km	Age at DSZ tip(f) km	T at DSZ tip(g) K	Max depth(h) km	Age at max depth(i) Ma	T at max depth(j) K
1 Alaska	59.7	-153.1	46	47	15	150	50	820	150 (8)	50	820
2 N. Chile	-21.5	-68.6	48	78	13	145	50	770	220 (3)	51	910
3 N. Sumatra	0.7	99.0	50	40	15	143	54	820	170 (9)	55	860
4 New Britain	-5.9	149.7	50	100	12	175	55	840	260 (4)	57	910
5 Kamchatka	51.2	156.8	100	76	29	196	103	820	250 (5)	104	830
6 Kermadec	-28.4	-177.9	100	57	30	230	107	820	300 (6)	109	840
7 NE Japan	38.7	141.4	130	83	34	195	133	870	300 (7)	134	880
8 Izu	34.0	140.2	140	51	36	162	145	870	300 (7)	149	880
9 S. Mariana	13.6	144.7	140	30	38	244	157	920	250 (8)	157	925

Notes:

(a) Locations of subduction zone segments are similar to those given in Ref (*1*).

(b) Slab age at the trench. All data are from Ref (*9*), except for New Britain, which is from (*10*).

(c) Subduction rate, in km/Ma. All data are from (*9*).

(d) Separation between UBS and LBS. All data are from Ref (*1*).

(e) Depth where UBS and LBS merge. Data from Ref (*1*), except for New Britain (*11*) and Kermadec (*12*).

(f) Slab age at the depth where UBS and LBS merge.

(g) Temperature in the LBS at the merging point.

(h) Maximum depth of intermediate-depth seismicity. Data sources are given for each entry. For old and cold slabs, no clear cut-off can be observed for intermediate-depth seismicity. Earthquake hypocenter distribution is continuous into the mantle transition zone. In those cases, we use 300 km as the cut-off.

(i) Slab age at the maximum depth of intermediate-depth seismicity.

(j) Temperatures at the maximum depths of intermediate-depth seismicity.

Table S2. Compositions (mol. %) of major phases in the starting material and experimental products.

Mineral	Opx[*]	Opx[†]	Grt[†]
SiO_2	48.78	47.65	42.60
TiO_2	0.08	0.02	0.07
Al_2O_3	2.07	2.08	10.99
FeO	14.57	13.80	18.38
MnO	0.11	0.01	0.01
MgO	33.92	36.01	22.22
CaO	0.44	0.38	5.69
Na_2O	0.03	0.03	0.03
Total	100	100	100

Notes:

[*] Starting material. FeO/(Mg+CaO+MnO+FeO)≈0.3.

[†] Reaction products after the experiments.

SI References

1. M. A. Florez, G. A. Prieto, Controlling Factors of Seismicity and Geometry in Double Seismic Zones. *Geophysical Research Letters* **46**, 4174-4181 (2019).
2. Q. Zhai, Z. Peng, M. Matsubara, K. Obara, Y. Wang, Systematic detections of intermediate-depth earthquakes in the subduction zone of central and northeastern Japan. *AGU Fall Meeting*, Abstract S035-0012 (2020).
3. C. Sippl, B. Schurr, T. John, S. Hainzl, Filling the gap in a double seismic zone: Intraslab seismicity in Northern Chile. *Lithos* **346-347**, 105155 (2019).
4. J. J. McGuire, D. A. Wiens, A double seismic zone in New Britain and the morphology of the Solomon Plate at intermediate depths. *Geophysical Research Letters* **22**, 1965-1968 (1995).
5. A. Gorbatov, V. Kostoglodov, G. Suárez, E. Gordeev, Seismicity and structure of the Kamchatka Subduction Zone. *Journal of Geophysical Research: Solid Earth* **102**, 17883-17898 (1997).
6. E. K. Todd, T. Lay, The 2011 Northern Kermadec earthquake doublet and subduction zone faulting interactions. *Journal of Geophysical Research: Solid Earth* **118**, 249-261 (2013).
7. L. M. Warren, E. C. Baluyut, T. Osburg, K. Lisac, S. Kokkinen, Fault plane orientations of intermediate-depth and deep-focus earthquakes in the Japan-Kuril-Kamchatka subduction zone. *Journal of Geophysical Research: Solid Earth* **120**, 8366-8382 (2015).
8. Z. Gui *et al.*, Spatiotemporal Seismotectonic Implications for the Izu ‐ Bonin ‐ Mariana Subduction Zone from b ‐ Values. *Seismological Research Letters* **91**, 1679-1693 (2020).
9. I. Wada, K. Wang, Common depth of slab-mantle decoupling: Reconciling diversity and uniformity of subduction zones. *Geochemistry, Geophysics, Geosystems* **10**, (2009).
10. E. Honza, H. L. Davies, J. B. Keene, D. L. Tiffin, Plate boundaries and evolution of the Solomon Sea region. *Geo-Marine Letters* **7**, 161-168 (1987).
11. S. S. Wei, D. A. Wiens, P. E. van Keken, C. Cai, Slab temperature controls on the Tonga double seismic zone and slab mantle dehydration. *Science Advances* **3**, e1601755 (2017).
12. H. Kawakatsu, Double seismic zone in Tonga. *Nature* **316**, 53-55 (1985).